Measurement of the liquid argon energy response to nuclear and electronic recoils

P. Agnes,[1,2] J. Dawson,[2] S. De Cecco,[3] A. Fan,[4] G. Fiorillo,[5,6] D. Franco,[2] C. Galbiati,[7] C. Giganti,[3] T. N. Johnson,[8,*] G. Korga,[1,9] D. Kryn,[2] M. Lebois,[10] A. Mandarano,[11,9] C. J. Martoff,[12] A. Navrer-Agasson,[3] E. Pantic,[8] L. Qi,[10] A. Razeto,[9] A. L. Renshaw,[1] Q. Riffard,[2,†] B. Rossi,[6] C. Savarese,[11,9] B. Schlitzer,[8] Y. Suvorov,[4,9] A. Tonazzo,[2] H. Wang,[4] Y. Wang,[4] A. W. Watson,[12] and J. N. Wilson[10]

(The ARIS Collaboration)

[1]*Department of Physics, University of Houston, Houston, Texas 77204, USA*
[2]*APC, Université Paris Diderot, CNRS/IN2P3, CEA/Irfu, Obs. de Paris, Sorbonne Paris Cité, Paris 75205, France*
[3]*LPNHE Paris, Sorbonne Université, Université Paris Diderot, CNRS/IN2P3, Paris 75252, France*
[4]*Department of Physics and Astronomy, University of California, Los Angeles, California 90095, USA*
[5]*Department of Physics, Università degli Studi Federico II, Napoli 80126, Italy*
[6]*Istituto Nazionale di Fisica Nucleare, Sezione di Napoli, Napoli 80126, Italy*
[7]*Department of Physics, Princeton University, Princeton, New Jersey 08544, USA*
[8]*Department of Physics, University of California, Davis, California 95616, USA*
[9]*Laboratori Nazionali del Gran Sasso, Assergi AQ 67010, Italy*
[10]*Institut de Physique Nuclaire Orsay, F91406 Orsay, France*
[11]*Gran Sasso Science Institute, L'Aquila 67100, Italy*
[12]*Department of Physics, Temple University, Philadelphia, Pennsylvania 19122, USA*

(Received 22 January 2018; published 19 June 2018)

A liquid argon time projection chamber, constructed for the Argon Response to Ionization and Scintillation (ARIS) experiment, is exposed to the highly collimated and quasimonoenergetic LICORNE neutron beam at the Institut de Physique Nucléaire d'Orsay (IPNO) in order to study the scintillation response to nuclear and electronic recoils. An array of liquid scintillator detectors, arranged around the apparatus, tag scattered neutrons and select nuclear recoil energies in the [7, 120] keV energy range. The relative scintillation efficiency of nuclear recoils is measured to high precision at null field, and the ion-electron recombination probability is extracted for a range of applied electric fields. Single-scattered Compton electrons, produced by gammas emitted from the deexcitation of $^7Li^*$ in coincidence with the beam pulse, along with calibration gamma sources, are used to extract the recombination probability as a function of energy and electron drift field. The ARIS results are compared with three recombination probability parametrizations (Thomas-Imel, Doke-Birks, and PARIS), allowing for the definition of a fully comprehensive model of the liquid argon response to nuclear and electronic recoils down to the few-keV range. The constraints provided by ARIS to the liquid argon response at low energy allow the reduction of systematics affecting the sensitivity of dark matter search experiments based on liquid argon.

DOI: 10.1103/PhysRevD.97.112005

I. INTRODUCTION

The field of direct dark matter searches has experienced a significant expansion in the past decade, with a growing number of experiments striving to increase the sensitivity to signals from dark matter particles. Direct dark matter search experiments seek a possible interaction between dark matter and Standard Model matter in specialized, low-background detectors deployed in underground laboratories. The absence of an unambiguous observation of weakly interacting massive particle (WIMP) signals in recent years has pushed experiments to increase their sensitivity by simultaneously reducing the background, enlarging the active detector volume, and lowering the energy threshold of the searches.

In this context, noble liquids are ideal candidates as target materials: they are relatively inexpensive, intrinsically more pure than other materials, and scalable to masses

*tesjohns@ucdavis.edu
†riffard@apc.in2p3.fr

 © 2018 American Physical Society

in the multiton range. Further, they are excellent scintillators (~40 000 photons/MeV) and good ionizers (10–30 eV ionization energy) in response to the passage of radiation.

Dual-phase noble liquid time projection chamber (TPC) detectors are currently the most sensitive detectors in searches for multi-GeV mass WIMPs [1–3]. The detection mechanism relies on the delayed coincidence between scintillation and ionization signals generated by the passage of an interacting particle. The prompt scintillation light (S1 signal) is produced by the decay of excited dimers of noble atoms, which are formed after one atom is excited. Interactions also produce ionization electrons, drifted by an electric field toward a gaseous region, where they produce a delayed light pulse by electroluminescence (S2 signal). A fraction of ionization electrons, however, recombine with ions to form excited dimers which contribute to S1 and deplete the S2 signal.

With respect to other noble liquid targets, liquid argon (LAr) exhibits a powerful rejection of electronic recoil backgrounds ($>10^8$ discrimination power [4]) through the temporal pulse shape of the scintillation signal. The combination of this pulse-shape discrimination technique and the use of argon extracted from deep underground, highly depleted in cosmogenic isotopes [5], makes liquid argon an ideal target for multiton detectors.

The sensitivity of liquid argon detectors can be enhanced by constraining the parameters of the liquid argon response to interacting particles, such as the quenching of nuclear recoils and the electron-ion recombination effect. These parameters are difficult to constrain in large detectors with external sources, because of the passive materials which suppress interactions in the target. Alternatively, the liquid argon response can be measured by auxiliary calibration experiments which exploit small-scale detector setups exposed to neutron and gamma beams. These experiments, tailored specifically for measurements of the liquid argon response, are able to accurately explore the low energy ranges for nuclear and electronic recoils under controlled conditions.

The Argon Response to Ionization and Scintillation (ARIS) experiment is a fixed kinematics scattering experiment utilizing a LAr TPC aimed to investigate the response of LAr to nuclear and electronic recoils, with nuclear recoils measured down to ~2 $\mathrm{keV_{ee}}$ (electron equivalent energy). The ARIS TPC is exposed to the LICORNE pulsed neutron source at the ALTO facility in Orsay, France [6]. The LICORNE source exploits the $^1\mathrm{H}(^7\mathrm{Li}, n)^7\mathrm{Be}$ inverse kinematic reaction, which guarantees a highly collimated and quasimonoenergetic (~1.5 MeV) neutron beam, and at the same time, monoenergetic gammas from the 478 keV $^7\mathrm{Li}^*$ deexcitation in coincidence with the beam pulse. Neutrons and gammas scattered in the TPC are detected by an array of eight liquid scintillator detectors (labeled A0 to A7) which constrain the recoil energy in the TPC through the detector angle with respect to the TPC-beam axis. A picture of the setup is shown in Fig. 1.

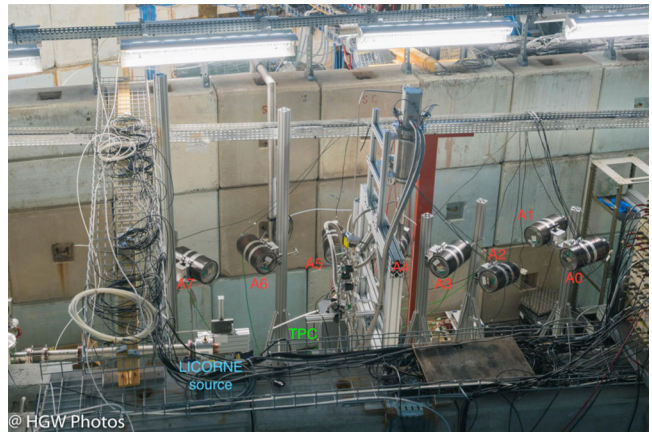

FIG. 1. Picture of the ARIS setup in the LICORNE hall.

In this work, we report on the precise measurement of the LAr scintillation efficiency for nuclear and electronic recoils at null field, and the dependence of the electron-ion recombination effect on the electric field.

II. EXPERIMENTAL SETUP

The ARIS TPC was designed to minimize nonactive materials in the direction of the neutron beam to inhibit interaction in passive materials. The ~0.5 kg LAr active mass is housed in a 7.6-cm inner diameter, 1-cm thick polytetrafluoroethylene (PTFE) sleeve. The PTFE inner surface includes an embedded enhanced specular reflector film for increased light reflection. The PTFE sleeve supports a set of 2.5-mm thick copper rings connected by resistors in series to maintain a uniform electric field throughout the active argon volume as depicted in Fig. 2. The TPC is held in a double-walled stainless steel dewar.

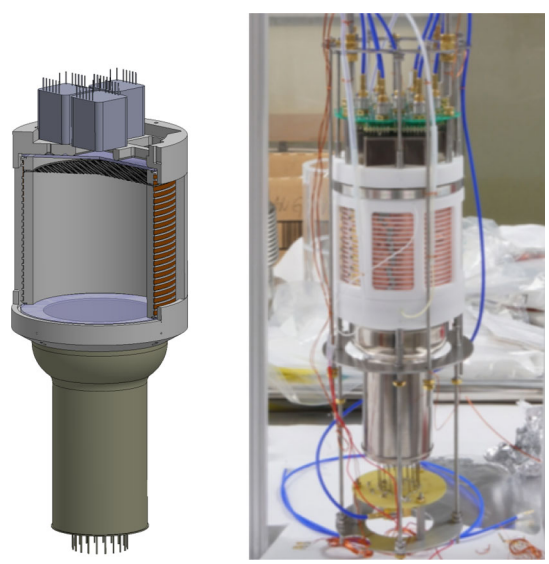

FIG. 2. Left panel: Three-dimensional drawing of the TPC. Right panel: Picture of the TPC.

Evaporated argon is continuously purified with a getter and recondensed by means of a custom cold head.

The electric field is created by two fused silica windows placed at the end caps of the cylindrical volume. The fused silica windows are coated with indium tin oxide which is a transparent conductor. A hexagonal stainless steel grid is placed 1 cm below the anode to enable the creation of an extraction field for a potential S2 signal. The anode is held at ground while the voltages on the extraction grid and cathode are tuned to create a uniform drift field across the entire liquid volume. The electric field uniformity was confirmed with COMSOL [7] simulations, with deviations smaller than 1% for all drift fields.

For the measurements presented in this paper, the TPC was operated in single phase without a gas pocket, in both the field-off and field-on regimes. This allows for a minimal data acquisition (DAQ) gate, leading to a reduced accidental background. In a dual-phase TPC, the gate length is dominated by the electron drift time, which depends on the electric field. By collecting only S1 signals, the gate can be reduced from tens/hundreds of microseconds to $\sim 10\ \mu$s. The amplitude of the ionization component can be inferred from the comparison of S1 signals with/without the electric field applied, as discussed in Sec. VIII.

The scintillation photons are wavelength shifted from the ultraviolet to visible range by the tetraphenyl butadiene compound, which has been evaporated onto all surfaces facing the active volume. Wavelength-shifted photons are observed by one 3-inch R11065 photomultiplier tube (PMT) below the cathode and seven 1-inch R8520 PMTs above the anode. An optical fiber connected to a LED, powered by a pulse generator, is used to calibrate the single photoelectron response of the PMTs.

The TPC is mounted with its center 1.00 m away from the LICORNE neutron production target, a hydrogen gas cell which is exposed to a ^{7}Li beam that can be accelerated to different energies. For the measurements presented in this paper the ^{7}Li energy was set at 14.63 MeV. The gas cell and the beam pipe are separated by a thin tantalum foil where ^{7}Li nuclei lose some of their energy. The determination of the ^{7}Li energy after passing through the tantalum foil and the parameters of the neutron beam are described in the next section. The ^{7}Li beam provides 1.5-ns wide pulses every 400 ns with a current between 20 and 40 nA. The neutrons reaching the TPC are of the order of 10^4 Hz.

The eight neutron detectors (NDs) surrounding the TPC have active volumes of NE213 liquid scintillator, with a diameter of 20 cm and a height of 5 cm [8]. The pulse shape of the signal from the liquid scintillator can be used to discriminate between neutrons and γ's. The NDs are located at distances from the TPC ranging from 1.3 to 2.5 m, oriented at angles between 25.5 and 133.1 degrees (see Table I). The ND positions were precisely measured before the data taking with a survey method yielding an accuracy of 2–3 mm, depending on the ND. An inspection after the data taking identified a mismatch between the recorded position of A2 and its position during data taking, which is reflected in a larger systematic uncertainty for measurements using that data point, described in further detail in Sec. VII.

TABLE I. Scattering angles, NR mean energies for neutrons from the ^{1}H(^{7}Li, n)^{7}Be reaction, and electron recoil (ER) mean energies from Compton-scattered γ's emitted by ^{7}Li* deexcitation, are shown. The scattering angle is defined with respect to the center of the NDs active surface while the mean energies are determined with Monte Carlo simulations.

	Scattering Angle [deg]	Mean NR Energy [keV]	Mean ER Energy [keV]
A0	25.5	7.1	42.0
A1	35.8	13.7	75.9
A2	41.2	17.8	85.8
A3	45.7	21.7	110.3
A4	64.2	40.5	174.5
A5	85.5	65.4	232.0
A6	113.2	98.1	282.7
A7	133.1	117.8	304.9

Data taking occurred during a 12 day period in October 2016 with various electric fields in the TPC, ranging from 0 to 500 V/cm. Data were taken in two modes: a double-coincidence mode between the beam pulse and a TPC trigger, and a triple-coincidence mode which included also coincidence with at least one of the NDs. The TPC trigger condition requires at least two PMTs to fire within 100 ns and a measurement of the TPC trigger efficiency will be described in Sec. IV. The triple coincidence data set provides nuclear (NR) and electronic recoils of defined energies. The double-coincidence data, which provides continuous spectra, are used for an investigation of the LAr scintillation time response, which will be presented in a future publication.

When a trigger occurs signals from the TPC PMTs and from A0–A7 are digitized by two CAEN V1720 boards at a 250 MHz frequency. The time of the beam pulses is also digitized at a 250 MHz frequency by a CAEN V1731 board. The board time stamps are synchronized by an external clock to allow for time-of-flight measurements.

For each coincidence, the TPC PMT waveforms, the ND waveforms, and the signal from the beam pulse are recorded. The acquisition window was 10 μs for the TPC PMTs and 7 μs for each ND. The signals are analyzed by a reconstruction software based on the ART framework [9] to extract observables from the recorded waveforms. First, fluctuations and drift of the baseline are tracked and subtracted from the raw signal waveforms. Next, waveforms from each PMT in the TPC are corrected for their single photoelectron response and summed together. A pulse-finder algorithm is applied to each summed waveform to identify the magnitude and start time of TPC and

ND pulses. Finally, the reconstructed waveform and pulse information are used to extract the S1 amplitude, pulse shape discrimination parameters for both the TPC and NDs, and time-of-flight (TOF) parameters.

A GEANT4-based Monte Carlo simulation of the experimental setup has been developed which includes the materials, size, and relative placement of the TPC, PMTs, dewar, and A0–A7 detectors as described above. The beam kinematics is also included as described in Sec. III. This simulation provides a spectrum of nuclear and electronic recoil energies from coincidences between the TPC and A0–A7 detectors, with mean values listed in Table I.

III. NEUTRON BEAM KINEMATICS

The LICORNE neutron beam exploits the inverse kinematic reaction resulting from accelerated ^{7}Li incident on a gaseous hydrogen target. The kinematics of the neutrons emitted from the $^1\mathrm{H}(^7\mathrm{Li}, n)^7\mathrm{Be}$ reaction highly depends on the energy of the ^{7}Li at the reaction site. The ^{7}Li beam is initially accelerated to 14.63 MeV, and a fraction of its energy is lost as it crosses the tantalum foil containing the hydrogen target. The exact thickness of the foil, and therefore the final ^{7}Li energy, is not well known. A dedicated measurement was performed to determine the ^{7}Li energy at the reaction site, and therefore the kinematic profile of the neutron beam. One ND was placed at a distance of 3 m from the source at angles varying between 0 and 15°. The relative neutron beam intensity with respect to the intensity at 0° was measured at each angle. The resulting profile was compared with the results of a GEANT4 simulation developed to predict neutron spectra as a function of ^{7}Li energy [10], which assumes different thicknesses of the tantalum foil.

The best fit of the beam profile was obtained for a foil thickness of 2.06 ± 0.08 μm, corresponding to a mean ^{7}Li energy in the hydrogen target of $13.13^{+0.02}_{-0.01}$ MeV. The corresponding kinematic profile of the neutron beam, in neutron energy vs angle with respect to the ^{7}Li beam axis, is shown in Fig. 3. The TPC, located 1 m from the neutron source, is exposed to <2° of the neutron cone. The mean neutron energy in this region is 1.45 MeV with an rms of 85 keV.

In addition to neutrons, LICORNE isotropically emits a source of 478 keV γ's in the center of mass frame from either the ^{7}Be decay or by the deexcitation of $^7\mathrm{Li}^*$, produced when ^{7}Li crosses the tantalum foil. The decay of ^{7}Be, with a half-life of ~53 days, constitutes a source of constant accidental background within the beam pulse. The $^7\mathrm{Li}^*$ γ's are emitted in coincidence with the beam pulse, and when detected in coincidence between the beam pulse, TPC, and a ND, provide an excellent source of single Compton electrons for investigating the LAr response to ERs. The $^7\mathrm{Li}^*$ γ's are subjected to a relativistic boost due to the motion of the $^7\mathrm{Li}^*$ nuclei, which increases their energy up to 6% for a ^{7}Li energy of 14.63 MeV. Since the $^7\mathrm{Li}^*$ energy at which γ's are emitted can vary because of the energy loss in the source materials, a mean boost of 3% and, conservatively, a σ of 3% are assumed, resulting in a γ energy of 492 ± 15 keV.

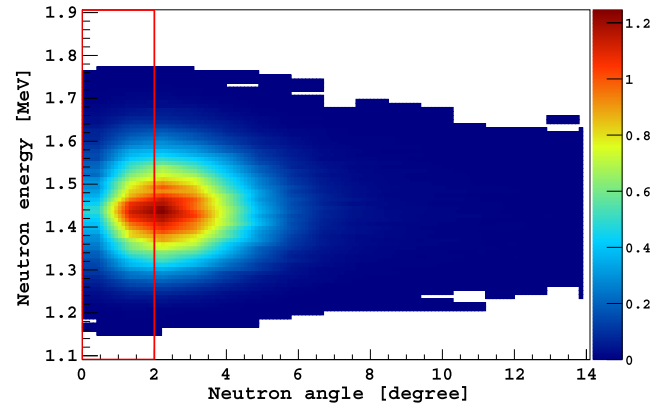

FIG. 3. Neutron kinematic profile for a ^{7}Li energy of 13.13 MeV incident on the hydrogen target, determined from Monte Carlo simulations. The red box defines the geometrical acceptance of the TPC.

IV. DETECTOR CALIBRATION

The TPC response to scintillation light was calibrated throughout the data-taking period with ^{241}Am and ^{133}Ba γ sources placed on the outside surface of the dewar. Dominant γ lines able to cross the dewar walls and reach the active LAr mass are 59.5 keV from ^{241}Am and 81.0–383.8 keV from ^{133}Ba.

The energy deposits of the γ's in the LAr active target are simulated with a GEANT4-based Monte Carlo program. Its output is converted to the S1 observable by convolving energy deposits in the LAr with a response function. The response function is generated with a toy Monte Carlo approach, taking into account the light yield (LY), Poisson fluctuations in the photon statistics, the nonuniformity of the light collection along the vertical axis, and the PMT response. The last is measured by fitting the single photoelectron distribution obtained with a pulsed LED light fed to the TPC through an optical fiber. The single photoelectron distribution was monitored throughout the data-taking period. The topological uniformity in light collection is measured by looking at the top/bottom asymmetry (TBA) observable, defined as the ratio between the light collected by the bottom PMT with respect to the total. The light collection is expected to be larger at the bottom because the 3-inch PMT provides a larger optical coverage and quantum efficiency with respect to the 1-inch PMT array at the top. The γ's from the ^{241}Am source are used to evaluate the dependence of the light collection on the TBA. In Fig. 4, the mean S1 of the ^{241}Am γ peaks observed in different

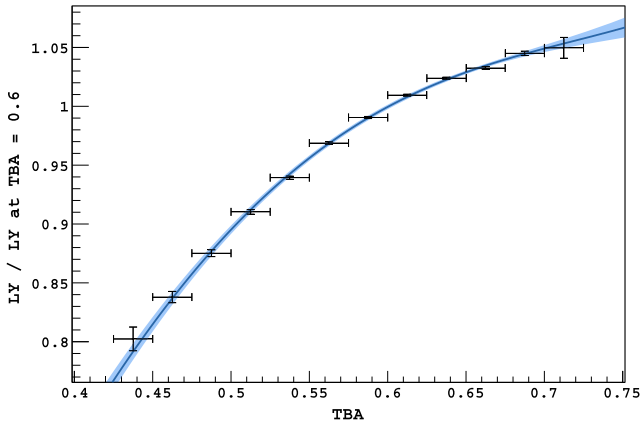

FIG. 4. Relative light collection efficiency as a function of the TBA. Larger values of TBA correspond to recoils closer to the bottom of the TPC.

subranges of TBA is shown with respect to S1 for TBA = 0.6. TBA = 0.6 corresponds to the mean value of the TBA for events induced by a source placed at the center of the TPC.

The ^{241}Am and ^{133}Ba data are then fit with the simulated distributions with the LY as the only free parameter. The ^{241}Am and ^{133}Ba spectra and best-fit Monte Carlo distributions are shown in Fig. 5. A $\chi^2/\mathrm{d.o.f.} \sim 1$ is achieved for both sources, showing that data and Monte Carlo are in excellent agreement. A slow 1.8% decrease in the LY over the period of data taking, likely due to variations in the LAr purity, was observed with daily calibrations with the γ sources, resulting in the dominant systematic error on the LY measurement. The best fit is obtained for $\mathrm{LY} = 6.35 \pm 0.05$ pe/keV with the uncertainty including the systematic error on the LY stability. The response map obtained for the average LY is shown in Fig. 6.

The trigger efficiency is derived with a dedicated measurement with a ^{22}Na source placed on the external wall of the dewar. ^{22}Na emits a positron, resulting in two back-to-back 0.511 MeV γ's, simultaneous with an isotropic 1.27 MeV γ. Two BaF_2 detectors were placed at a distance of ~2 cm from the source: one on the TPC-^{22}Na source axis in order to detect one of the two 0.511 MeV γ's from the positron annihilation, and the second rotated by about 45 degrees with respect to the same axis to detect the isotropic 1.27 MeV γ. This trigger configuration provides a selection of events where one 0.511 MeV γ is directed toward the TPC center when both BaF_2 detectors are triggered. In this case, the TPC event and the TPC trigger status (two or more PMTs fire within 100 ns) are recorded along with the light collected in the two BaF_2 detectors. Offline cuts on the BaF_2 signals optimize the selection of 0.511 MeV γ rays directed toward the TPC center, inducing a Compton electron spectrum ensuring a trigger efficiency scan over the entire energy range of interest. A dependence of the trigger efficiency on the TBA is expected due to the

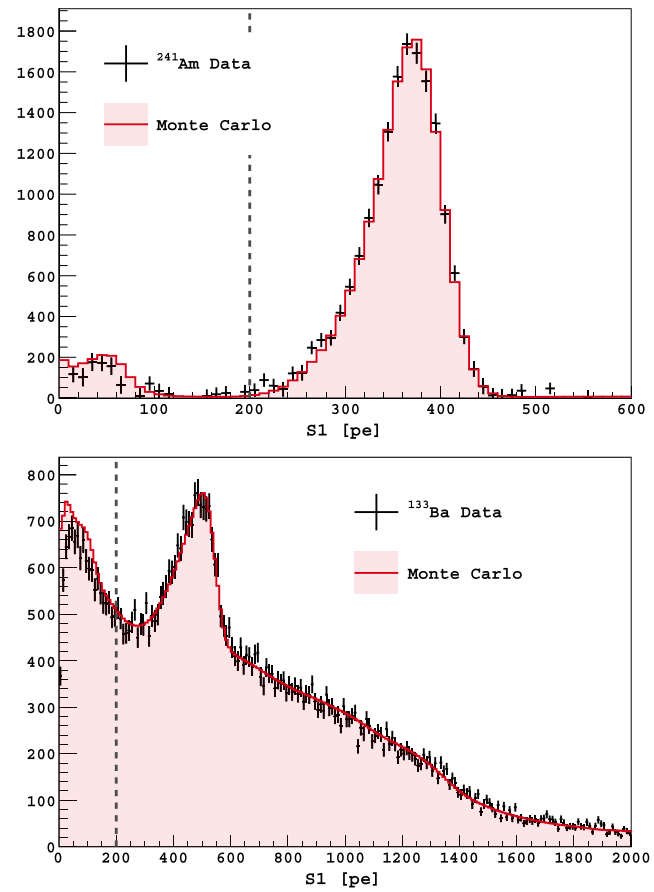

FIG. 5. ^{241}Am (top) and ^{133}Ba (bottom) spectra from source calibration of the TPC light yield at 0 V/cm with an overlay of the best-fit spectra. The χ^2/d.o.f. is 20.7/29 for ^{241}Am and 190.7/189 for ^{133}Ba. The vertical dashed line represents the low threshold for the fit interval.

asymmetry in the photosensor setup on the top and bottom of the TPC and the trigger condition.

The trigger efficiency is measured as a function of the signal in the first 100 ns ($S1_{100}$), the same gate as the one

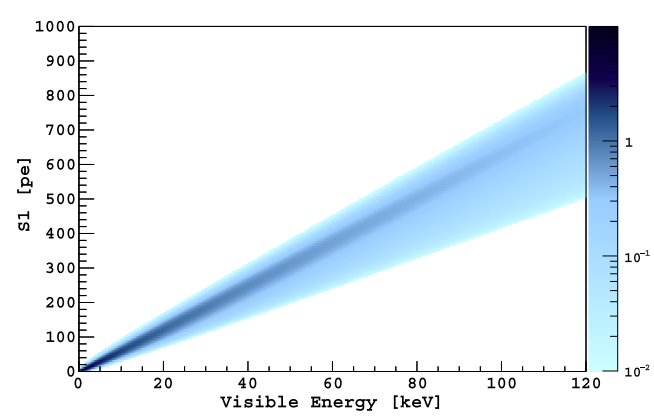

FIG. 6. The TPC optical response as a function of visible energy defined from the toy Monte Carlo approach described in the text.

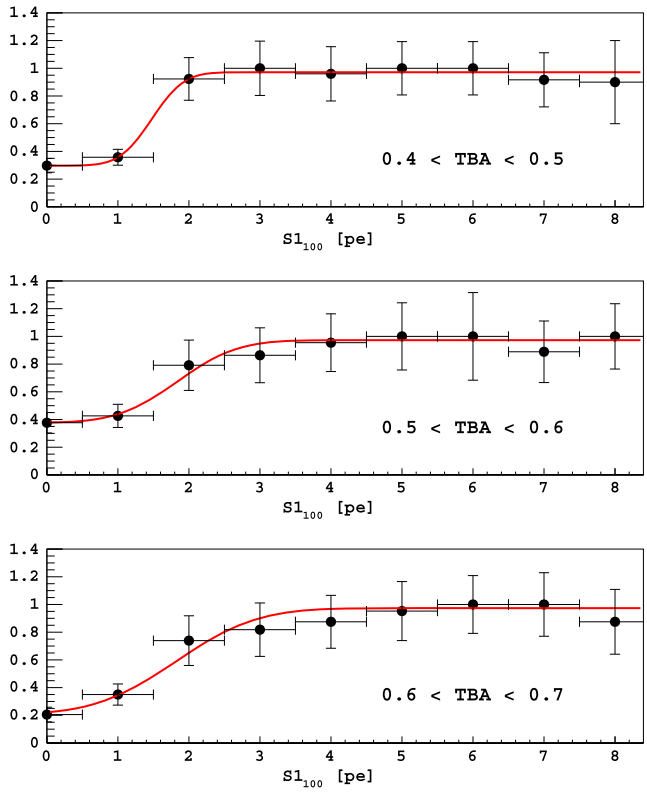

FIG. 7. The trigger efficiency, as a function of $S1_{100}$, measured with the ^{22}Na source for three regions of TBA. The plateau at high energies does not reach unity due to the inhibition time of 10 ms introduced after each trigger. Dark noise prevents the efficiency from reaching zero at very low values of $S1_{100}$.

used for the trigger. Monte Carlo simulations have demonstrated that ER and NR have the same trigger efficiency with respect to this variable. The fraction of reconstructed events with a positive trigger status as a function of $S1_{100}$ is evaluated for three regions of TBA, approaching 1 in the entire detector for $S1_{100} > 6$, as shown in Fig. 7. Beam data are corrected on an event-by-event basis by evaluating the corresponding $S1_{100}$ value. Figure 8 shows the comparison of corrected and uncorrected NR spectra selected by coincidence with the A0 detector (7.1 $\mathrm{keV_{nr}}$), where the impact of the trigger efficiency is maximal.

The TPC saturation has been investigated with the ^{22}Na source by comparing S1 with $S1_{\mathrm{late}}$, the integral of the signal starting after the first 90 ns. This integral range is not affected by saturation since it is dominated by the slow component of the scintillation emission with a characteristic time of $\sim 1.6\ \mu$s. A deviation from the linearity between S1 and $S1_{\mathrm{late}}$ is observed from $S1 = 4000$ pe, corresponding to more than 600 $\mathrm{keV_{ee}}$. A similar study has been performed on the spectrum of NRs selected in the double-coincidence trigger mode. The prompt scintillation component in NRs is larger than for ERs, so the effect of saturation is expected at lower S1. Up to 400 pe, corresponding to the maximum energy of NRs induced by

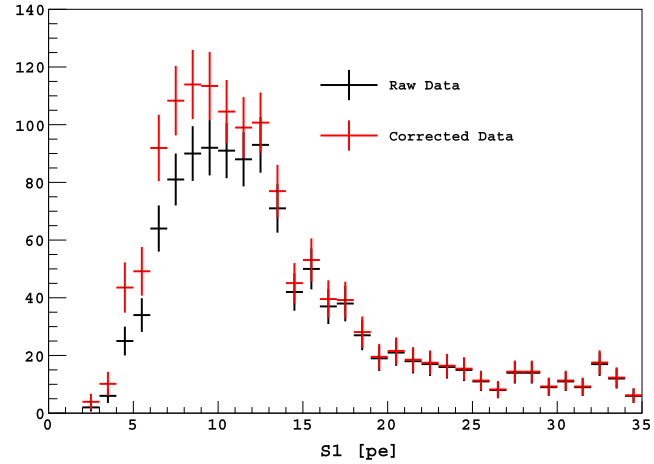

FIG. 8. The effect of the trigger efficiency correction on the NR energy spectrum for events selected by coincidence with A0, resulting in a mean NR energy of 7.1 $\mathrm{keV_{nr}}$. The impact of the trigger efficiency is maximal for this data point.

1.45 MeV neutrons, no deviations from linearity were observed between S1 and $S1_{\mathrm{late}}$.

A clock misalignment was occasionally observed on a run-by-run basis between the CAEN boards. To synchronize them, a time calibration for each run was performed using the $^{7}\mathrm{Li}^{*}\ \gamma$ signal from the triple-coincidence trigger data. The TOF between the beam pulse and the TPC ($\mathrm{TOF_{TPC}}$) and the beam pulse and the NDs ($\mathrm{TOF_{ND}}$) is shown in Fig. 9, compared with Monte Carlo simulations

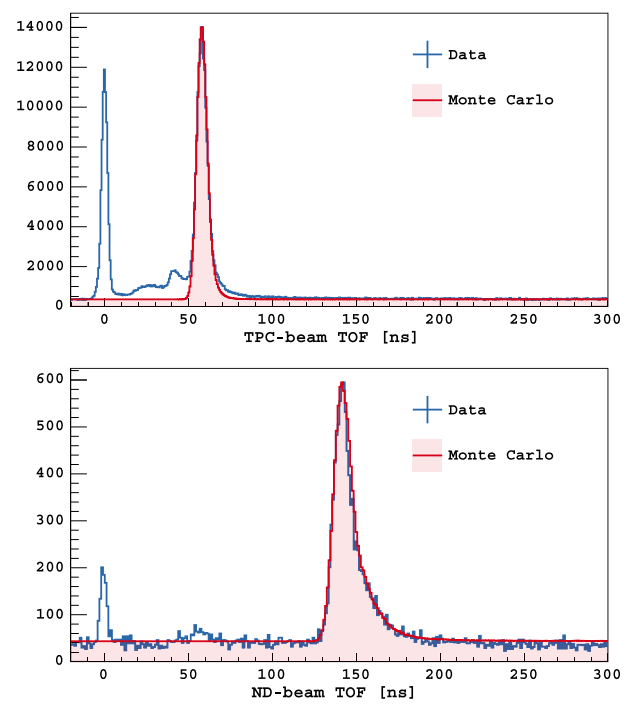

FIG. 9. Data and Monte Carlo comparisons of the $\mathrm{TOF_{TPC}}$ (top) and $\mathrm{TOF_{ND}}$ (bottom) distributions for the A3 detector. The peak at 0 ns corresponds to the $^{7}\mathrm{Li}^{*}\ \gamma$ that are not simulated in the MC.

of neutrons for the A3 ND. The time resolutions of the two TOFs are measured with ^{7}Li* γ's to be 1.8 ns for the TOF_{TPC}, and in the 2–3 ns range for the eight TOF_{ND} and are included in the simulation. The excellent agreement in both TOF distributions is an indirect confirmation of the neutron kinematic profile assumed in the Monte Carlo simulation.

V. SELECTION CRITERIA

In order to understand the different populations of events in the data sample, four observables are used: the two previously defined TOF variables (TOF_{TPC} and TOF_{ND}), and the TPC (f_{90}) and ND (PSD_{ND}) pulse-shape variables. f_{90} is defined as the fraction of the first 90 ns of the light pulse in the TPC, while PSD_{ND} corresponds to the fraction of photoelectrons detected after 40 ns up to the end of the acquisition gate (7 μs) in the NDs.

Figure 10 shows different combinations of observables for triple-coincidence events in the A3 ND, highlighting four different classes of events as well as the selection cuts for NR and ER signals. The four classes of events described in the subsequent paragraphs are labeled in the figure.

D1: A large f_{90} indicates that these events are mostly NRs, and the values of $TOF_{TPC} \sim 60$ ns and $TOF_{ND} \sim 150$ ns are in agreement with the expected TOF from ~1.5 MeV neutrons traveling 1 m to the TPC and 2.5 m to the ND. The PSD_{ND} variable confirms that these events are neutrons, with a mean value of ~0.35 corresponding to the expectation for proton recoil in a scintillator from a neutron interaction.

D2: The small f_{90} and PSD_{ND} in combination with TOF values at the few-nanosecond scales provide clear indications that these events are beam-generated γ's interacting in both the TPC and ND.

D3: f_{90} classifies these events as neutrons, but the two TOFs are shorter than for the expected signal from ~1.5 MeV neutrons. These high-energy neutrons are identified as byproducts of fusion-evaporation reactions between the different target materials and the accelerated ^{7}Li.

D4: The short TOF_{ND}, compatible with γ's in the ND, and the long TOF_{TPC}, compatible with neutrons in the TPC, identify these events as accidental coincidences between a neutron and γ correlated with the beam pulse.

Events in the D1 and D2 categories are selected by combining cuts on the TOF_{TPC}, TOF_{ND}, and PSD_{ND} variables. The selection has been optimized independently for each ND. As an example, the cuts used for A3 are shown by the red boxes in Fig. 10. The f_{90} cut is excluded by the data selection to avoid possible biases in the TPC energy spectra due to the correlation between S1 and f_{90}.

The most significant background to the neutron signal population is from accidental coincidences between a neutron in the TPC and an ambient γ in a ND. A probability density function of the S1 spectrum of this background is produced by selecting events with the same TOF_{TPC} as is used for the D1 signal events, accepting all events in the TOF_{ND} variable that are not coincident with the D1 or D2 region windows. The background spectrum is normalized to a high-energy region of the signal S1 spectrum for NR events, by requiring S1 > 500 pe, and subtracted, as shown in the top plot of Fig. 11 for the ND A3.

In the case of ERs, γ's scattering multiple times in the TPC materials is the dominant background, making accidental background subtraction irrelevant. The overall background is estimated using the *TSpectrum Background*

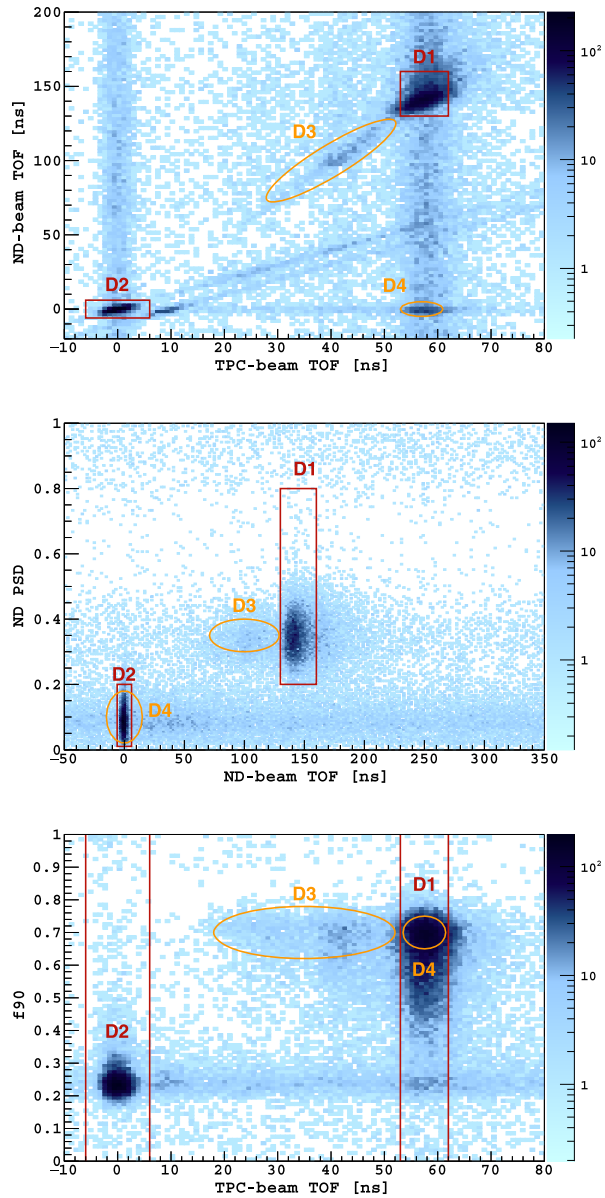

FIG. 10. TOF_{ND} vs TOF_{TPC} (top), PSD_{ND} vs TOF_{ND} (center), and f_{90} vs TOF_{TPC} (bottom) for triple coincidences with the A3 detector. The numbered populations are described within the text. The red lines correspond to the selection cuts for NRs (D1) and ERs (D2). Yellow lines highlight two classes of NR (D3) and ER backgrounds.

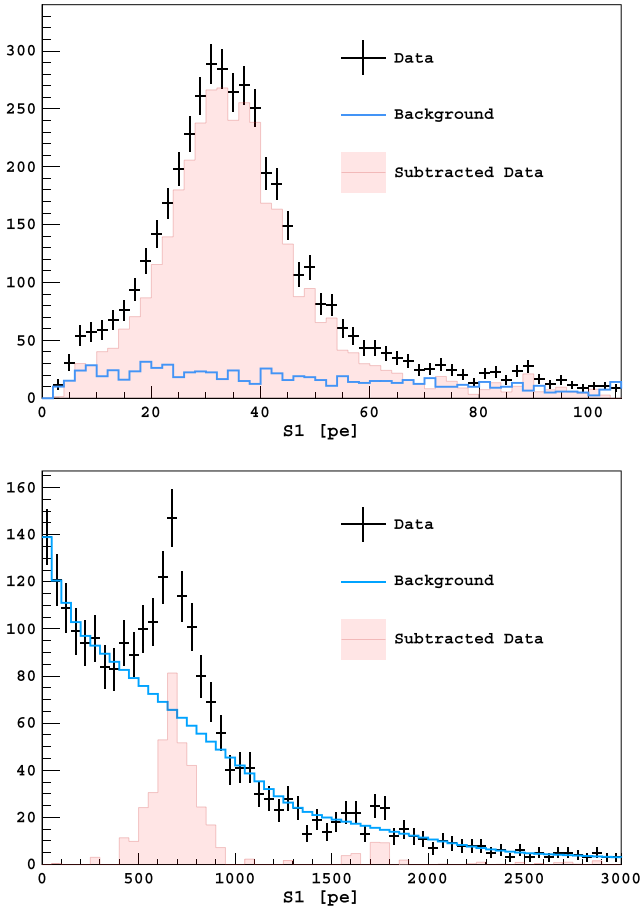

FIG. 11. Top: NR spectrum in A3 (21.5 keV recoil energy). Bottom: ER spectrum for Compton electrons in A3. In black is the spectrum after all the selection cuts. The background is represented by the blue histogram.

algorithm from ROOT [11], as shown in the bottom plot of Fig. 11 for A3.

VI. RESPONSE TO ELECTRON RECOILS AT NULL FIELD

Existing measurements [12] suggest that the LAr response at null field to ERs is linear and hence not subjected to energy-dependent quenching effects, unlike what has been observed in liquid xenon [13]. Previous measurements of the linearity of the ER response in LAr have relied on multiple-scatter sources, such as the multistep decay of ^{83m}Kr and γ sources in the Compton-scattering-dominated regime. Direct measurements from single electronic recoils have not yet confirmed the linearity.

The eight single ER energies from Compton scattering of the monoenergetic γ emitted by the ^{7}Li* deexcitation, tagged with the eight NDs, are ideal candles for this test. Data from the TPC is background subtracted as described in Sec. V, and the resulting peak is fit with a Gaussian function. The LY for Compton scatters tagged by NDs is evaluated as a function of the Compton electron energy determined with Monte Carlo simulation. The LY of each ND tagged data set is found relative to the mean value of the set of eight measurements, and the relative LY's are fit with a first-degree polynomial resulting in a maximum deviation from unity of 5% in the [41.5, 300] keV range. The value of this deviation includes the statistical error from the fit.

The LY values independently extracted from the full absorption γ peaks, shown in Fig. 12, from ^{241}Am (59.5 keV), ^{133}Ba (81 and 356 keV), and ^{22}Na (511 keV), are fully compatible with the average LY derived from single Compton electrons. This is expected for the full absorption peaks of 59.5 and 81 keV γ's as they are dominated by the photoelectric effect. The 356 and 511 keV γ interactions, instead, are dominated by Compton scattering, producing multiple lower-energy electrons. If they were subjected to a quenching that is stronger at low energies (as it is the case, for example, for organic liquid scintillator), the light yield derived from multiple-scatter γ's should differ from the one derived from single-scatter events.

Fitting simultaneously the ^{241}Am, ^{133}Ba, ^{22}Na, and Compton electrons, the LY in the [41.5, 511] keV range is constant within 1.6%, as shown in Fig. 12. This result confirms the linearity of the LAr scintillation response at null field also observed by Lippincott *et al.* [12] at 3%, using multiple-scatter sources in the [41.5, 662] keV range. This result suggests that, at null field, ERs are not subjected to nonlinear quenching effects and that calibrations of LAr detectors can be performed either with single- or multiple-scatter ER sources without introducing any bias.

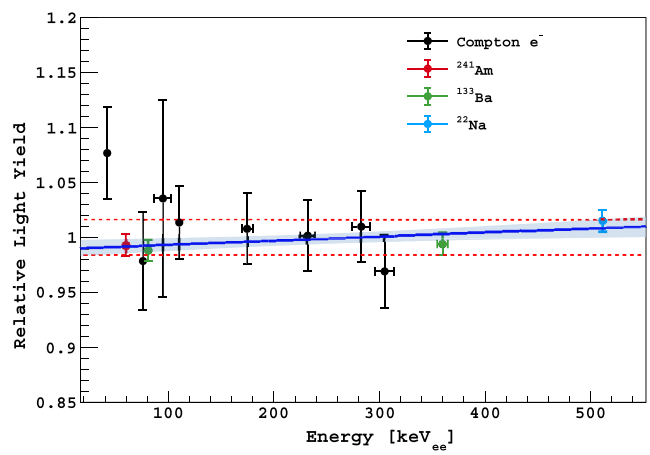

FIG. 12. The relative LY, with respect to the mean, as a function of the Compton electron energy from ^{7}Li* deexcitation, and from ^{241}Am (59.5 keV), ^{133}Ba (81 and 356 keV), and ^{22}Na (511 keV) γ sources. The vertical error bars represent the statistical errors on LY while the horizontal error bars represent the uncertainties on the energy. All the data points are fit with a first-degree polynomial (blues line) to test for deviations from unity. The dashed red lines correspond to $\pm 1.6\%$ bands and contain the fitted polynomial, including 1σ error (blue band), in the [41.5, 511] keV range.

VII. RESPONSE TO NUCLEAR RECOILS AT NULL FIELD

The scintillation efficiency for nuclear recoils, $\mathcal{L}_{\rm eff}$, is defined in this work with respect to the response of LAr to the 59.5 keV γ from ^{241}Am at null field. The comparison with other $\mathcal{L}_{\rm eff}$ measurements [14–16] using different reference sources (e.g., ^{57}Co and ^{83m}Kr) is guaranteed by the linearity of the ER response demonstrated in the previous section.

S1 distributions of NR data samples, selected with a coincidence signal from each ND as described in Sec. V, are independently fit with a probability density function derived from the Monte Carlo simulation. The only free parameters in the fit are the normalization factor and $\mathcal{L}_{\rm eff}$, which acts as a scaling factor of the light yield. Results from each fit are shown in Fig. 13.

The sources of systematic error affecting this measurement are listed in Table II. The dominant contributions to the uncertainty on $\mathcal{L}_{\rm eff}$ are the uncertainties on the LY and on the ND positions. The first is evaluated with an analytical propagation of the error on the LY, while the second relies on Monte Carlo simulations where the ND positions were varied according to the uncertainty from the survey in the direction that maximizes the NR energy spread. The survey was done by measuring the distance of each ND from several reference points along the beam direction. An *a posteriori* cross-check was done by overlaying several photographs of the entire setup with the rendering of the geometry in the Monte Carlo simulation using the BLENDER software [17]. The TPC, the source position, and the ND support structures were used as reference anchors in the comparison. All ND positions were confirmed within a maximum shift of 4 cm with the exception of A2, which required a shift of $(-6, +7, +13)$ cm with respect to the survey position.[1] The size of the shift is conservatively assumed to be the uncertainty on the A2 position and, when propagated to the NR energy, results in an uncertainty of 5.5%. The uncertainty on the NR energy for coincidences with the other NDs ranges from 0.8% to 2.5%.

Other subdominant sources of systematic error relating to the setup geometry and materials are the uncertainties on the ^{7}Li energy, with its determination described in Sec. III, and the TPC position, known within 1 cm. Their impact on $\mathcal{L}_{\rm eff}$, quoted in Table II, was evaluated with Monte Carlo simulations. Systematic effects associated with the analysis procedure, such as the trigger efficiency correction, the TOF cuts, histogram binning, energy range of the fit, and background subtractions were investigated by varying the associated parameters. Only the uncertainties on the trigger efficiency and the TOF selection induce a non-negligible systematic error on $\mathcal{L}_{\rm eff}$ and are quoted in Table II.

[1] x is the beam-TPC direction, z is the vertical coordinate, and y is orthogonal to the x-z plane.

This work provides the most precise determination of the $\mathcal{L}_{\rm eff}$ dependence on the NR energy in LAr, as shown in Fig. 14, where it is compared with previous measurements [14–16] in LAr.

These results can be compared with the quenching models for LAr proposed by Mei [18], which predicts a quenching factor of

$$\mathcal{L}_{\rm eff}^{M} = f_n \times \frac{1}{1 + k_B \frac{dE}{dx}}, \tag{1}$$

where, f_n is the ionization energy reduction factor due to losses to the nuclear stopping power, as predicted by Lindhard model [19]. The Mei model derives $k_B = 7.4 \times 10^{-4}$ MeV^{-1} g cm^{-2} from heavy-ion measurements. Figure 15 shows, however, that this model does not accurately reproduce ARIS data. The Mei model is disfavored at 2σ even using k_B as a free parameter in a fit. The agreement is recovered by adding a quadratic term,

$$\mathcal{L}_{\rm eff}^{M*} = f_n \times \frac{1}{1 + k_B \frac{dE}{dx} + k_B^{*}(\frac{dE}{dx})^2}, \tag{2}$$

as in the extended version of the Birks formula for organic scintillators [20]. In this way, the model is compatible with the data with a p-value of 0.79 as shown in Fig. 15, and the best-fit parameters are $k_B = (5.2 \pm 0.6) \times 10^{-4}$ MeV^{-1} g cm^{-2} and $k_B^{*} = (-2.0 \pm 0.7) \times 10^{-7}$ MeV^{-2} g^2 cm^{-4}. This result is in agreement with the best fit of the modified Mei model to DarkSide-50 data which yields a value of $k_B = (4.66^{+0.86}_{-0.94}) \times 10^{-4}$ MeV^{-1} gcm^{-2} [21].

VIII. S1 RESPONSE VS ELECTRIC FIELD

In addition to the null-field data set, data were acquired at 50, 100, 200, and 500 V/cm drift fields in triple-coincidence mode. The presence of an electric field in the active volume increases the probability that ionization electrons escape the electron-ion cloud, reducing the recombination effect.

Any energy deposit in LAr produces an average number of quanta ($N_{\rm q}$), either excitons or ion-electron pairs, corresponding to

$$N_{\rm q} = N_{\rm i} + N_{\rm ex} = \mathcal{L}_{\rm eff} \times \frac{E_{\rm dep}}{W} \tag{3}$$

where $W = 19.5$ eV [22] is the effective work function, $N_{\rm ex}$ and $N_{\rm i}$ are the number of excitons and ions, respectively, and $\mathcal{L}_{\rm eff}$ is assumed to be 1 for ERs. S1 can be expressed as function of α, the $N_{\rm ex}/N_{\rm i}$ ratio:

$$S1 = \epsilon_1(\alpha + R) \times N_{\rm i} \tag{4}$$

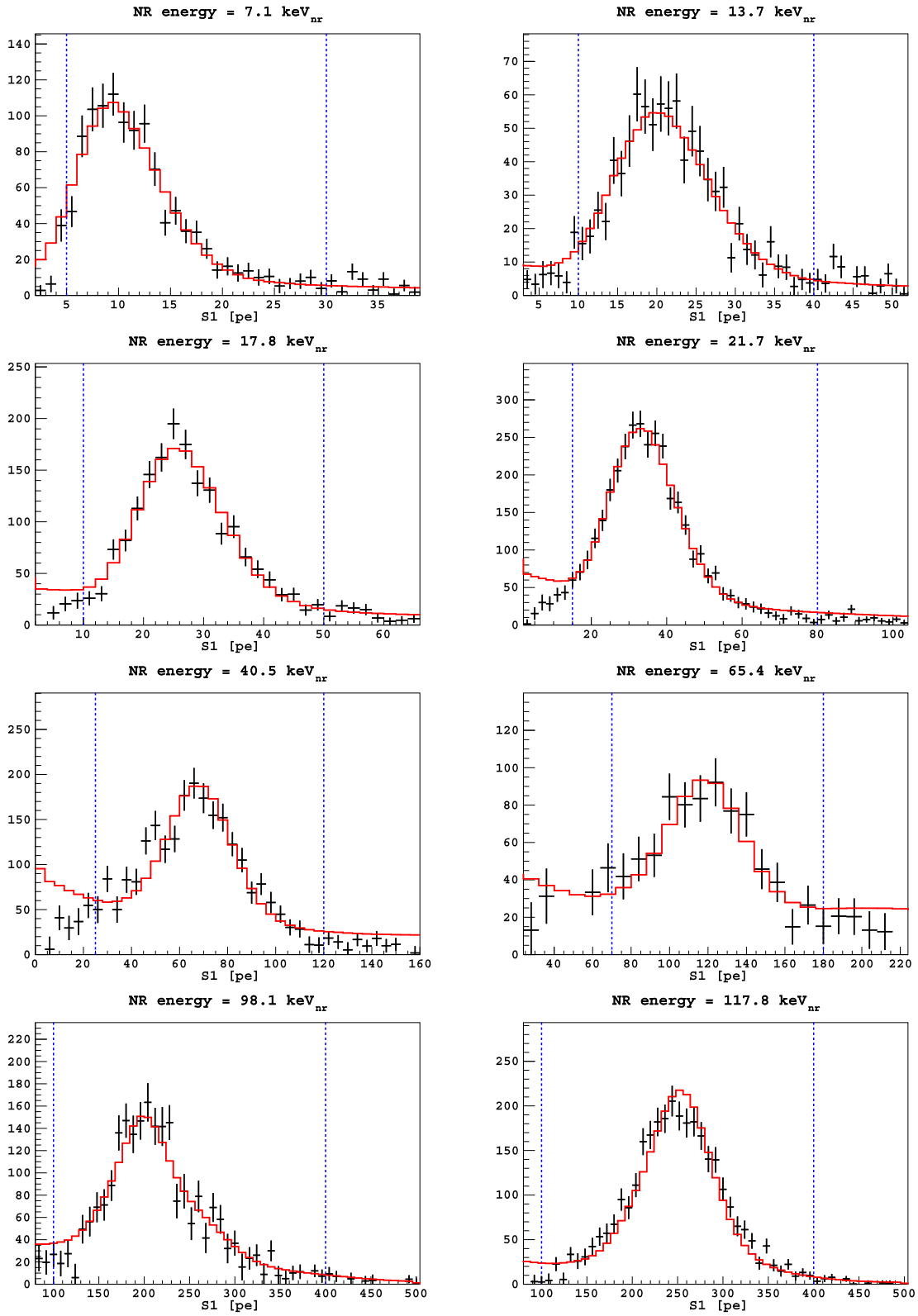

FIG. 13. Nuclear recoil data taken with zero electric field, fitted with the Monte-Carlo-derived probability density functions for events in coincidence with the A0-7 detectors (red lines). The vertical dashed lines indicate the fitting range for each spectrum.

TABLE II. Measured $\mathcal{L}_{\rm eff}$ for NR events coincident with each ND with the different sources of systematic uncertainties and the statistical uncertainty from the fit quoted.

NR energy [keV]	7.1	13.7	17.8	21.7	40.5	65.4	98.1	117.8
$\mathcal{L}_{\rm eff}$	0.243	0.258	0.253	0.269	0.286	0.304	0.332	0.349
Light-yield	0.002	0.002	0.002	0.002	0.002	0.002	0.003	0.003
Beam kinematic	0.001	0.002	$o(10^{-3})$	$o(10^{-3})$	$o(10^{-3})$	$o(10^{-3})$	$o(10^{-3})$	$o(10^{-3})$
A0–A7 position	0.006	0.005	0.014	0.005	0.004	0.004	0.003	0.003
TPC position	$o(10^{-3})$	$o(10^{-3})$	$o(10^{-3})$	$o(10^{-3})$	$o(10^{-3})$	$o(10^{-3})$	$o(10^{-3})$	$o(10^{-3})$
A0–A7 TOF	$o(10^{-3})$	$o(10^{-3})$	0.001	0.001	$o(10^{-3})$	0.002	0.001	0.001
TPC TOF	0.002	0.001	0.001	0.001	0.002	0.002	0.002	0.002
Trigger efficiency	$o(10^{-3})$	$o(10^{-3})$	$o(10^{-3})$	$o(10^{-3})$	$o(10^{-3})$	$o(10^{-3})$	$o(10^{-3})$	$o(10^{-3})$
Total Syst.	0.007	0.006	0.014	0.006	0.005	0.005	0.005	0.005
Stat.	0.005	0.004	0.003	0.002	0.003	0.006	0.004	0.002
Combined	0.009	0.007	0.015	0.006	0.006	0.008	0.006	0.005
Combined relative [%]	3.8	2.7	5.8	2.3	2.1	2.6	1.8	1.5

where ϵ_1 is the light collection efficiency of the detector, and R the electron-ion recombination probability. The value of α is equal to 0.21 for ERs, and to 1 for NRs [22].

In ARIS, the recombination dependences on electron recoil equivalent energy ($E_{\rm ee}$)[2] and field (F) are studied with respect to the observable

$$\frac{S1}{S1_0} = \frac{\alpha + R(E_{\rm ee}, F)}{1+\alpha}, \tag{5}$$

where $S1_0$ is the scintillation response at null field.

Equation (5) is expected to reproduce ARIS data in both ER and NR modes, by accordingly changing the value of α, if the recombination probability $R(E,F)$ is correctly modeled. The $S1/S1_0$ ratio extracted from the data is compared with three recombination models: the Thomas-Imel [23], Doke-Birks [22], and PARIS models [21]. The first is an extension of the Jaffe "box" theory [24] and was demonstrated to be accurate in the "short track" regime, such as NRs or low-energy ERs. The Doke-Birks model is empirical and expected to reproduce data at higher energies. The PARIS model was tuned on DarkSide-50 data at 200 V/cm only, but was demonstrated to work from ~3 keV up to ~550 keV.

The Doke-Birks model parametrizes R as follows:

$$R = \frac{AdE/dx}{1+BdE/dx} + C, \tag{6}$$

where $B = A/(1-C)$ and dE/dx is the energy loss by electrons in LAr. We introduce a dependence on the electric field, F, by defining

$$C = C' e^{-D\times F}. \tag{7}$$

ARIS data in ER mode were simultaneously fit with this electric-field-modified version of the Doke-Birks model in the $[40, 300]$ keV$_{\rm ee}$ range, with the results shown in Fig. 16. The parameters returned by the fit are $A = (2.5 \pm 0.2) \times 10^{-3}$ cm/MeV, $C' = 0.77 \pm 0.01$, and $D = (3.5 \pm 0.3) \times 10^{-3}$ cm/V. With these parameters, the model is able to reproduce ER data with energy from 40 keV at any field. However, while the Doke-Birks recombination tends to 1 at lower energies, observations from the DarkSide-50 data demonstrate that it should decrease [21]. The PARIS model, which was designed to solve this issue, does not require any tuning of the parameters and accurately matches the data, as shown in Fig. 17. The difference between the Doke-Birks and PARIS models appears for energies below 10 keV$_{\rm ee}$.

NR data, converted into ER equivalent energy by means of the $\mathcal{L}_{\rm eff}$ measured in Sec. VII, are fit with the

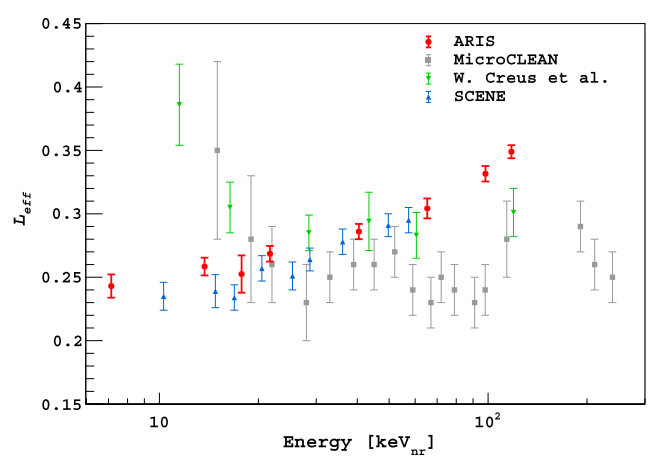

FIG. 14. $\mathcal{L}_{\rm eff}$ dependence on NR energy as measured by this work and compared with other data sets [14–16].

[2]In the case of NRs, $E_{\rm ee} = \mathcal{L}_{\rm eff}(E_{\rm nr}) \times E_{\rm nr}$.

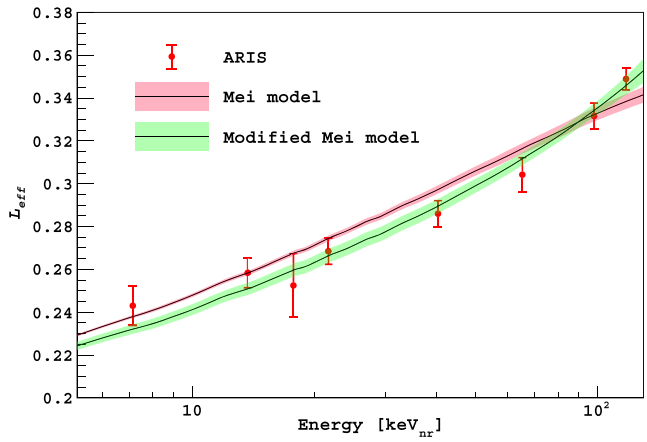

FIG. 15. $\mathcal{L}_{\rm eff}$ values measured by this work fit with Mei and modified Mei models as described by Eqs. (1) and (2) in the text.

Thomas-Imel model, in which the recombination probability is given by

$$R = 1 - \frac{\ln(1+\xi)}{\xi}, \tag{8}$$

where

$$\xi = C_{\rm box}\frac{N_i}{F^{\beta}}. \tag{9}$$

$C_{\rm box}$ is a constant depending on the mean ionization electron velocity v and on the size of the ideal box containing the electron-ion cloud.

Figure 18 shows the $S1/S1_0$ ratio, at different fields, for NRs, fit with the Thomas-Imel model. The fit returns $\beta = 1.07 \pm 0.09$, in good agreement with the Thomas-Imel prediction of $\beta = 1$, and $C_{\rm box} = 18.5 \pm 9.7$. The resulting Thomas-Imel model for NRs is compared with the Doke-Birks and PARIS models under the paradigm that, with a

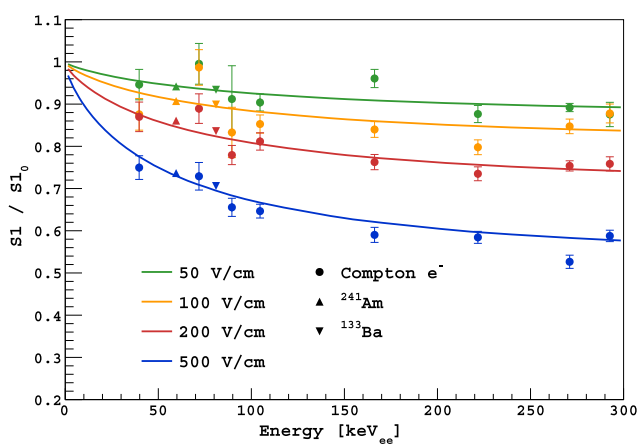

FIG. 16. Field induced quenching of S1 for ERs at different drift fields, fit with the Doke-Birks model.

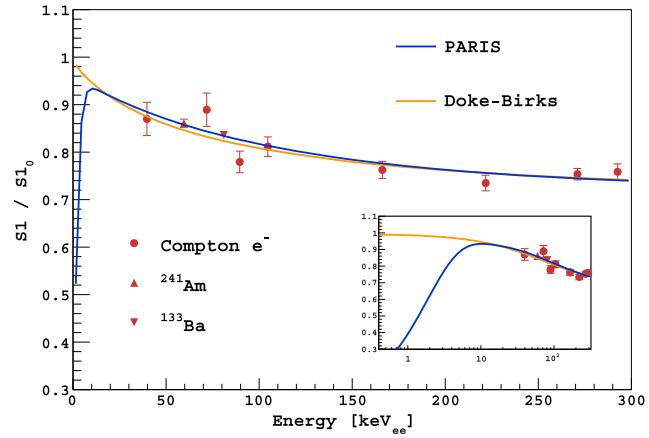

FIG. 17. Field-induced quenching of S1 for ERs at 200 V/cm compared with the PARIS model and the fit of the Doke-Birks model. The inset shows the same data with the x axis represented on a log scale.

fixed recombination probability, models should be able to describe both ER and NR data sets by changing the scintillation-to-ionization ratio from $\alpha = 0.21$ (ER) to $\alpha = 1$ (NR). This paradigm is disproved by the comparison between models and the NR data set at 200 V/cm, shown in Fig. 19, where Doke-Birks and PARIS predictions are rejected at more than 5σ. The Doke-Birks and PARIS models are not recovered in NR mode, even by changing the α value.

An overall model requires then two separate recombination probabilities in order to describe both ERs and NRs. In the range of dark matter searches in LAr (<60 keV$_{\rm ee}$), the tuned Thomas-Imel model correctly describes scintillation response to NRs, while the PARIS model is confirmed as a good model for ERs, if operating at 200 V/cm. The Doke-Birks model provides a good description of ERs

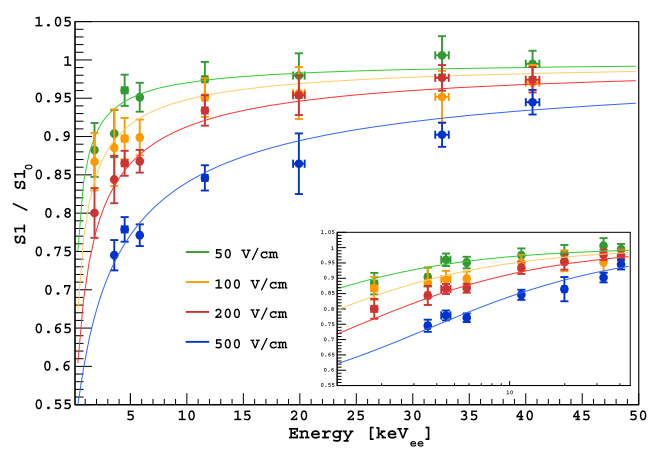

FIG. 18. Field-induced quenching of S1 for NRs for different drift fields fit with the Thomas-Imel model. The systematic uncertainties are included in the error bars. The inset shows the same data with the x axis represented on a log scale.

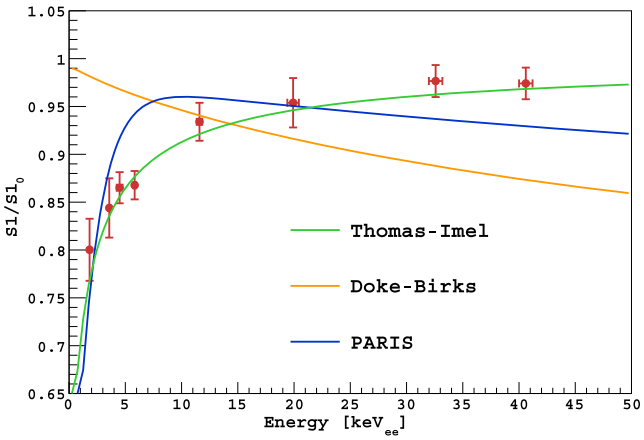

FIG. 19. Field-induced quenching of S1 for NRs at 200 V/cm compared to model predictions from the Thomas-Imel model, tuned on the NR data set, and Doke-Birks and PARIS models, tuned on ERs, assuming $\alpha = 1$.

at different fields, but almost outside the range of interest (>40 keV$_{ee}$) for dark matter searches.

As a final check, the tuned Thomas-Imel model is used to predict the number of ionization electrons escaping the recombination

$$N_e = \mathcal{L}_{\mathrm{eff}} \times \frac{E_{\mathrm{dep}}}{W} \frac{1 - R(E_{\mathrm{ee}}, F)}{1 + \alpha} \tag{10}$$

measured by Joshi *et al.* [25], as function of the drift field (F), for 6.7 keV$_{nr}$ NRs, assuming the $\mathcal{L}_{\mathrm{eff}}$ measured in this work. Figure 20 shows excellent agreement, suggesting that, apart from $\mathcal{L}_{\mathrm{eff}}$, no extra-quenching factor affects S2, which can be essentially modeled as complementary to S1, under the assumption that the excitation-to-ionization ratio α is equal to 1 for NRs.

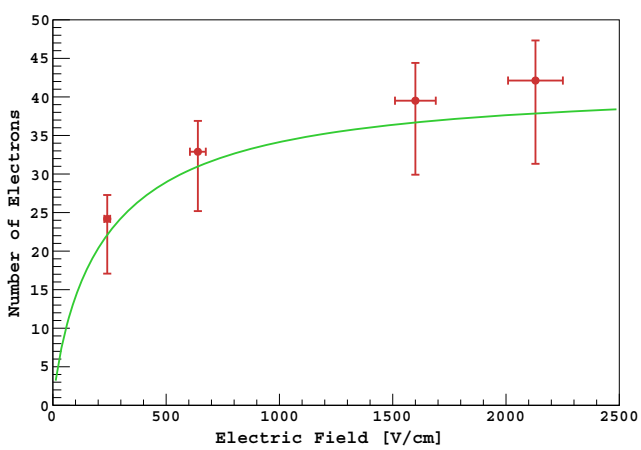

FIG. 20. Comparison of the S2 signal, expressed in number of ionization electrons, between the Joshi *et al.* data set at 6.7 keV$_{nr}$ and the Thomas-Imel model prediction, as a function of the drift field.

IX. CONCLUSIONS

The scintillation yield of nuclear recoils relative to electronic recoils between ~7 and ~120 keV$_{nr}$ has been measured in LAr using a highly collimated and quasimonoenergetic neutron source. This work presents the most precise measurement and lowest-energy probe of $\mathcal{L}_{\mathrm{eff}}$, the nuclear recoil scintillation efficiency in LAr.

In addition, Compton electrons induced by γ's from ^{7}Li*] deexcitation, in coincidence with the neutron beam, were used to measure the relative scintillation LY as a function of energy and drift field along with γ's from calibration sources. At null field, the LY was measured to be constant within 1.6% in the $[40, 511]$ keV$_{ee}$ range, the most stringent test of the linearity of the LAr response. Furthermore, no differences were observed in the light response between single- and multi-scatter ER events.

In the presence of an electric field, three models (Thomas-Imel, Doke-Birks, and PARIS) were compared to the NR and ER data sets. The Thomas-Imel electron-ion recombination probability function, properly tuned on these data, provides a good description of the response to NRs at different fields, while the PARIS model was confirmed as a good model for ERs at the DarkSide-50 operation drift field of 200 V/cm. The Doke-Birks recombination probability models the response to ERs at different fields, but only above 40 keV$_{ee}$, in the upper range of interest for dark matter searches.

Finally, a comparison of the ionization signal between the tuned Thomas-Imel model and an independent NR data set at 6.7 keV$_{nr}$ suggests that no extra quenching factors are required to predict the number of ionization electrons.

In conclusion, this work provides a fully comprehensive model of the LAr response in the range of interest for dark matter searches through the measurement of the $\mathcal{L}_{\mathrm{eff}}$ parameter as a function of NR energy, and by properly tuning the parametrization of the electron-ion recombination probabilities for ERs and NRs.

Recent analyses of DarkSide-50 have extended by up to an order of magnitude the exclusion region for WIMP-nucleus interactions in the WIMP mass range below 6 GeV/c^2 [26], and slightly improved limits for WIMP-electron interactions, assuming a heavy mediator [27]. To achieve these results, the DarkSide-50 Collaboration has benefited from the ARIS results by better constraining the response of nuclear recoils in LAr in both field-on and field-off configurations. The linearity of the electron recoil scintillation response measured by ARIS has allowed DarkSide-50 to derive the spectral shape of forbidden ^{39}Ar β decay, an important cosmogenic background intrinsic to LAr. The ARIS results have then impacted both of the analyses by improving signal and background models.

ACKNOWLEDGMENTS

The ARIS Collaboration would like to thank Institut de Physique Nucléaire d'Orsay and its staff for invaluable technical and logistical support. We also thank Stephen Pordes for providing electronic boards. This report is based upon work supported by the National Science Foundation (Grants No. PHY-1242585, No. PHY-1242611, No. PHY-1314501, No. PHY-1314483, No. PHY-1314507, and No. PHY-1455351) and the France-Berkeley Fund (2016-0053). We acknowledge the financial support from the UnivEarthS Labex program of Sorbonne Paris Cité (ANR-10-LABX-0023 and ANR-11-IDEX-0005-02).

[1] E. Aprile *et al.*, arXiv:1705.06655.
[2] D. S. Akerib *et al.*, Phys. Rev. Lett. **118**, 021303 (2017).
[3] A. Tan *et al.*, Phys. Rev. Lett. **117**, 121303 (2016).
[4] P. A. Amaudruz *et al.* (DEAP Collaboration), Astropart. Phys. **85**, 1 (2016).
[5] P. Agnes *et al.*, Phys. Rev. D **93**, 081101 (2016).
[6] J. Wilson, M. Lebois, P. Halipre, S. Oberstedt, and A. Oberstedt, Phys. Procedia **59**, 31 (2014).
[7] COMSOL Multiphysics Reference Manual, version 4.4 (COMSOL, Inc., Burlington, MA, 2013).
[8] H. Laurent, H. Lefort, D. Beaumel, Y. Blumenfeld, S. Fortier, S. Galès, J. Guillot, J. C. Roynette, P. Volkov, and S. Brandenburg, Nucl. Instrum. Methods Phys. Res., Sect. A **326**, 517 (1993).
[9] C. Green, J. Kowalkowski, M. Paterno, M. Fischler, L. Garren, and Q. Lu, J. Phys. Conf. Ser. **396**, 022020 (2012).
[10] M. Lebois, J. N. Wilson, P. Halipré, B. Leniau, I. Matea, A. Oberstedt, S. Oberstedt, and D. Verney, Nucl. Instrum. Methods Phys. Res., Sect. A **735**, 145 (2014).
[11] R. Brun and F. Rademakers, Nucl. Instrum. Methods Phys. Res., Sect. A **389**, 81 (1997).
[12] W. H. Lippincott, S. B. Cahn, D. Gastler, L. W. Kastens, E. Kearns, D. N. McKinsey, and J. A. Nikkel, Phys. Rev. C **81**, 045803 (2010).
[13] E. Aprile, C. E. Dahl, L. de Viveiros, R. J. Gaitskell, K. L. Giboni, J. Kwong, P. Majewski, K. Ni, T. Shutt, and M. Yamashita, Phys. Rev. Lett. **97**, 081302 (2006).
[14] D. Gastler, E. Kearns, A. Hime, L. C. Stonehill, S. Seibert, J. Klein, W. H. Lippincott, D. N. McKinsey, and J. A. Nikkel, Phys. Rev. C **85**, 065811 (2012).
[15] H. Cao *et al.*, Phys. Rev. D **91**, 092007 (2015).
[16] W. Creus, Y. Allkofer, C. Amsler, A. D. Ferella, J. Rochet, L. Scotto-Lavina, and M. Walter, J. Instrum. **10**, P08002 (2015).
[17] BLENDER, http://www.blender.org.
[18] D.-M. Mei, Z.-B. Yin, L. C. Stonehill, and A. Hime, Astropart. Phys. **30**, 12 (2008).
[19] J. Lindhard, V. Nielsen, M. Scharff, and P. V. Thomsen, Det Kgl. Danske Viden. **33**, 10 (1963).
[20] D. Smith, R. Polk, and T. Miller, Nucl. Instrum. Methods Phys. Res., Sect. A **64**, 157 (1968).
[21] P. Agnes *et al.* (DarkSide), J. Instrum. **12**, P10015 (2017).
[22] T. Doke, H. J. Crawford, A. Hitachi, J. Kikuchi, P. J. Lindstrom, K. Masuda, E. Shibamura, and T. Takahashi, Nucl. Instrum. Methods Phys. Res., Sect. A **269**, 291 (1988).
[23] J. Thomas and D. A. Imel, Phys. Rev. A **36**, 614 (1987).
[24] G. Jaff, Ann. Phys. (Berlin) **347**, 303 (1913).
[25] T. H. Joshi *et al.*, Phys. Rev. Lett. **112**, 171303 (2014).
[26] P. Agnes *et al.* (DarkSide Collaboration), arXiv:1802.06994.
[27] P. Agnes *et al.* (DarkSide Collaboration), arXiv:1802.06998.